The Astrophysical Journal, 823:96 (17pp), 2016 June 1 doi:10.3847/0004-637X/823/2/96

SOAR OPTICAL AND NEAR-INFRARED SPECTROSCOPIC SURVEY OF NEWLY DISCOVERED MASSIVE STARS IN THE PERIPHERY OF GALACTIC MASSIVE STAR CLUSTERS I-NGC 3603

A. Roman-Lopes[1], G. A. P. Franco[2], and D. Sanmartim[3]
[1] Department of Physics and Astronomy—Universidad de La Serena, Cisternas 1200, La Serena, Chile; aroman@userena.cl
[2] Departamento de Física—ICEx—UFMG, Caixa Postal 702, 30.123-970, Belo Horizonte, MG, Brazil
[3] Southern Astrophysical Research Telescope (SOAR), Chile
Received 2015 October 26; accepted 2016 March 31; published 2016 May 26

ABSTRACT

In this work, we present the results of a spectroscopic study of very massive stars (VMSs) found outside the center of the massive stellar cluster NGC 3603. From the analysis of the associated Southern Astrophysical Research (SOAR) Telescope spectroscopic data and related optical–near-IR (NIR) photometry, we confirm the existence of several VMSs in the periphery of NGC 3603. The first group of objects (MTT58, WR42e, and RF7) is composed of three new Galactic exemplars of the OIf*/WN type, all of them with probable initial masses well above 100 $M_{\odot}$ and estimated ages of about 1 Myr. Based on our Goodman blue-optical spectrum of another source in our sample (MTT68), we can confirm the previous finding in the NIR of the only other Galactic exemplar (besides HD 93129A) of the O2If* type known to date. Based on its position relative to a set of theoretical isochrones in a Hertzprung–Russel (H–R) diagram, we concluded that the new O2If* star could be one of the most massive (150 $M_{\odot}$) and luminous ($M_V = -7.3$) O-stars in the Galaxy. Also, another remarkable result is the discovery of a new O2v star (MTT31), which is the first exemplar of that class so far identified in the Milk Way. From its position in the H–R diagram it is found that this new star probably had an initial mass of 80 $M_{\odot}$, as well as an absolute magnitude of $M_V = -6.0$, corresponding to a luminosity similar to other known O2v stars in the Large Magellanic Cloud. Finally, we also communicate the discovery of a new Galactic O3.5If* star (RFS8) that is quite an intriguing case. Indeed, it is located far to the south of the NGC 3603 center, in apparent isolation at a large radial projected linear distance of ∼62 pc. Its derived luminosity is similar to that of the other O3.5If* (Sh18) found in NGC 3603's innermost region, and the fact that a such high mass star is observed so isolated in the field led us to speculate that perhaps it could have been expelled from the innermost parts of the complex by a close fly-by dynamical encounter with a very massive hard binary system.

Key words: stars: individual (MTT31, MTT58, MTT68, MTT71, WR42e, HD 93129A)

1. INTRODUCTION

Very massive stars (VMSs) (Vink et al. 2015) are expected to be found in the core of their host clusters, generally forming binary or multiple stellar systems. Indeed, it is well accepted that the majority of massive stars are formed in clusters, with O3 stars having been considered, for a long time, the most massive hydrogen core burning stellar type. However, the situation has changed in the last few decades, as we now know that some hydrogen-rich nitrogen sequence Wolf–Rayet (WR) stars are in reality extremely massive and luminous main-sequence (MS) stars, which, because of their proximity to the Eddington limit, mimic the spectral appearance of classical WR stars, showing an emission line spectrum even at the beginning of their MS evolution (de Koter et al. 1997; Schnurr et al. 2008; Smith & Conti 2008; Crowther et al. 2010).

Several observational studies of the stellar masses of very massive binary systems indicate that such massive stellar objects belong to the OIf*/WNh and WNh spectral types (Smith et al. 1996; Smith & Conti 2008; Crowther et al. 2010; Crowther & Walborn 2011), making them the most massive MS stars known in the local universe. Evidence supporting this assumption comes from systematic studies of binaries made by Rauw et al. (1996) for WR22 (minimum masses of 71.7 ± 2.4 $M_{\odot}$ + 25.7 ± 0.8 $M_{\odot}$), Rauw et al. (2004) and Bonanos et al. (2004) for WR20a (two O3If*/WN6 stars with absolute masses of 83 $M_{\odot}$ and 82 $M_{\odot}$), Niemela et al. (2008) for WR21a (a WN6ha star with a minimum mass of 87 $M_{\odot}$ + O-type secondary with a minimum mass of 53 $M_{\odot}$), Schnurr et al. (2008) for NGC 3603-A1 (minimum masses of 116 ± 31 $M_{\odot}$ + 89 ± 16 $M_{\odot}$), and Schnurr et al. (2009) for R145 (minimum masses of 116 ± 33 $M_{\odot}$ + 48 ± 20 $M_{\odot}$). Finally, Crowther et al. (2010) found from their spectroscopic re-analyses of OIf*/WN and WNh stars in the cores of NGC 3603 and R136 in the Large Magellanic Cloud (LMC) that some stars there might have had initial masses in the range of 105–170 $M_{\odot}$ and 165–320 $M_{\odot}$, respectively.

Surprisingly, some VMSs are found in isolation in the field. As examples we can mention the cases of WR21a (a binary with minimum masses 87 $M_{\odot}$ + 53 $M_{\odot}$; Niemela et al. 2008) in Westerlund 2 (Wd2), WR42e (an O3If*/WN6 with an estimated initial mass above 100 $M_{\odot}$; Roman-Lopes 2012; Gvaramadze et al. 2013) in NGC 3603, and VFTS 682 in the LMC whose blue-optical spectrum looks very similar to that of R136a3 (one of the WNh stars found in the center of R136, with an inferred initial mass of ∼150–200 $M_{\odot}$; Bestenlehner et al. 2011; Vink et al. 2015). In this sense, there is a growing number of VMSs that are seen outside the cluster cores, sometimes found far away from their supposed parental clusters, perhaps forming massive stellar halos like the one seen in the field of the 30 Dor starburst region in the LMC (Walborn & Blades 1997; Walborn et al. 2014). In the Milk Way, this phenomenon seems to occur in the periphery of massive stellar clusters like Wd2 and NGC 3603, in which some of the most massive stellar members are found far from the cluster centers. For example, in Wd2, in addition to WR20a, there are WR20b (WN6ha) (Moffat et al. 1991; Shara

Table 1
Number of O2If*, OIf*/WN and WNh Stars Previously Known in the Wd2 and NGC 3603 Fields, Found at R_c Distances at Intervals $R_1 = (0 < R_c < r)$, $R_2 = (r < R_c < r_t)$, and $R_3 = R_c > r_t$

Cluster	r_c (′)	r (′)	r_t (′)	[0−r]	[r−r_t]	[>r_t]
Wd2	0.2	1.78	4.8	1	1	3
NGC 3603	0.05	2.0	14.6	7	1	0

Note. The parameters r_c, r, and r_t are, respectively, the observed cluster core radius, the cluster radius, and the cluster tidal radius of NGC 3603 and Wd2 derived by Hur et al. (2014) and Sung & Bessell (2004).

et al. 1991) and WR21a (WN6 + early-O) (Niemela et al. 2008), which are found in isolation at angular radial cluster center distances (R_c) of 0.′6, 3.′7, and 16′, respectively, plus two O2If*/WN6 stars, WR20aa and WR20c (Roman-Lopes et al. 2011), placed at large R_c values of 15.′7, and 25′, respectively. In NGC 3603's field there are three exemplars, MTT58 (O2If*/WN6), MTT68 (O2If*) and WR42e (O2If*/WN6), at R_c values of 1.′0, 1.′4, and 3′, respectively (Roman-Lopes 2012, 2013a, 2013b).

For comparison, in Table 1 we show the number of VMSs found in the direction of Wd2 and NGC 3603, tabulated for R_c values in the ranges $0 < R_c < r$, $r < R_c < r_t$, and $R_c > r_t$, with r and r_t being the observed cluster radius and the cluster tidal radius, respectively, taken from Hur et al. (2014) and Sung & Bessell (2004). We can see that the number of O2If*, OIf*/WN, and WNh objects found inside the circular area limited by the cluster radius r is higher in NGC 3603 than in Wd2, perhaps reflecting differences in the total mass of each cluster and/or in their dynamical evolutionary stages. However, no such objects are found beyond the area projected by the respective tidal radii, a behavior that led us to wonder if there were other VMSs still to be discovered on the outskirts of the NGC 3603 complex.

In this work we performed a search for VMS candidates placed beyond the center of the massive stellar cluster NGC 3603, which is known to be one of the most massive, dense, and rich Galactic star-forming regions (Melnick et al. 1989; Moffat et al. 2002; Sung & Bessell 2004), and possibly a scaled version of the starburst R136 cluster in the LMC (Andersen et al. 2009; Rochau et al. 2010). It has several massive stars in its core, many of them apparently showing initial masses up to 100–170 $M_\odot$ (Crowther et al. 2010). Based on near-infrared (NIR) color and magnitude selection criteria applied to objects found in the 2MASS point source catalog (2MASS PSC; Skrutskie et al. 2006), the chosen stars were surveyed through a Southern Astrophysical Research (SOAR) Telescope NIR spectroscopic survey with the aim to confirm their possible massive nature. The earliest stars selected from our analysis of the respective NIR spectra were then re-studied and spectroscopically re-classified using new SOAR–Goodman blue-optical data, resulting in the confirmation of the existence of several new massive stars in the NGC 3603 field.

2. NIR MAGNITUDE AND COLOR-RATIO SELECTION CRITERIA

The stars in this work were selected from the study of the NIR magnitudes and colors of sources in the 2MASS PSC found on the annular sky area (centered on the NGC 3603's coordinates) of internal and external radius 0.′5, and 35′, respectively, and presenting K_S-band magnitudes in the range $8.5 < K_S < 10$ and magnitude errors <0.1. For the sources matching the mentioned spatial and magnitude criteria, we kept those showing colors and color-ratios in the range $0.5 < (J–K_S) < 1.5$ and $1.5 < [(J–H)/(H–K_S)] < 2.0$, respectively, which in turn were defined based on the fact that massive stars are known to emit a lot of excess radiation in the infrared and radio domains, mainly due to the free–free emission generated by their powerful stellar winds (for more on this see Lamers & Cassinelli 1999 and references therein). In this sense, the K_S-band magnitude range and color criteria were tuned based on those of WR42e (O2If*/WN6), MTT58 (O2If*/WN6), and MTT68 (O2If*), with the K_S-band magnitude limit ($K_S = 10$) being fixed considering the maximum integration time previously assigned per source (about 30–35 minutes) with the Ohio State Infrared Imager and Spectrometer (OSIRIS) at SOAR, taking into account a minimum signal-to-noise ration (S/N) = 100 in the same spectral band. This empirical limit possibly results in a bias toward the most luminous (and potentially massive) objects, which in principle is not an issue as our main goal is to apply it to the most promising candidates. However, by using the mentioned magnitude limits we will probably miss several mid- to late-O-type stars. Indeed, as an example of this we can mention the case of the newly discovered O6v runaway star 2MASS J11171292-6120085 (Gvaramadze et al. 2013) which was found at 15.′6 from NGC 3603's center, and is not selected by our methodology because its K_S magnitude (10.92) is well above the assumed upper selection limit. We will also probably miss a certain number of massive stars positioned in the innermost regions of the complex, e.g., those with radial distances $r < 0.'5$.

From the application of the above criteria, about thirty 2MASS point sources were selected. Two of them are the known WR stars WR42c and WR42d (both of the WN5 type; Rosslowe & Crowther 2015), placed at NGC 3603 radial distances of 15′ and 6′, respectively. On the other hand, in the innermost regions there are two known O-stars, SHER 22 (O2-O3 III) and SHER 23 (OC9.7 Ia), both found less than 0.′5 from the NGC 3603 center. The 10 most extreme objects of the remaining selected sources are the subject of this paper. Their coordinates and photometric parameters, together with their assigned spectral types and NGC 3603 radial distances, are listed in Table 2. In Figure 1 we present a colorized *Spitzer* image centered on the NGC 3603 complex, in which we indicate the position of each selected source (shown by labels and arrows), as well as their relative position to the NGC 3603, NGC 3576, and NGC 3590 star formation complexes.

3. SPECTROSCOPIC DATA

In this section we present details of the observations and data reduction process of the OSIRIS NIR and Goodman optical spectroscopic data taken at the Southern Astrophysical Research (SOAR) Telescope for sources listed in Table 2. All but one of them (RFS10) were observed with both instruments. Our strategy was to observe the sources selected from the photometric criteria, first through the NIR window using OSIRIS, because many of the science targets are relatively faint at the U- and V-bands, mainly due to the large heliocentric distances combined with heavier interstellar absorption. The typical integration time necessary to obtain a

Table 2
List of Stars Observed with OSIRIS and Goodman with the SOAR Telescope

Source	R.A.(J2000)	Decl.(J2000)	B	V	J	H	K_S	r (arcmin–pc)	OSIRIS Data	Comments
RFS1	11:15:06.68	−61:16:33.3	15.29	14.07	10.67	10.17	9.86	0.7–1.5	Optical+NIR	MTT31[a] (O4V-O5V and X-ray)
RFS2	11:15:07.58	−61:16:54.6	16.14	14.76	10.47	9.68	9.24	1.0–2.1	Optical+NIR	MTT58 (X-ray)
RFS3	11:14:59.48	−61:14:33.8	16.31	14.72	9.98	9.17	8.74	1.4–3.0	Optical+NIR	MTT68 (X-ray)
RFS4	11:15:21.32	−61:15:04.3	16.31	14.74	10.60	9.99	9.60	1.8–3.7	Optical+NIR	MTT71 (X-ray)
RFS5	11:14:45.50	−61:15:00.1	16.05	14.53	10.18	9.47	9.04	3.0–6.4	Optical+NIR	WR42e (X-ray)
RFS6	11:14:53.55	−61:24:22.8	16.02	14.52	10.64	10.06	9.73	8.5–18	Optical+NIR	X-ray source
RFS7	11:15:15.36	−60:51:17.6	14.17	12.89	9.85	9.39	9.12	25–53	Optical+NIR	⋯
RFS8	11:16:12.62	−61:43:54.2	15.31	14.68	10.61	9.92	9.48	29–62	Optical+NIR	⋯
RFS9	11:12:53.35	−60:50:45.2	14.98	13.62	10.55	10.06	9.83	30–64	Optical+NIR	⋯
RFS10	11:19:55.12	−61:16:03.7	15.21	13.86	10.54	10.03	9.66	35–74	Optical	X-ray source

Notes. Column 1 is the assigned ID, Columns 2 and 3 their coordinates (J2000), Columns 4 and 5 the B- and V-band photometry taken from Sung & Bessell (2004) and Zacharias et al. (2004, 2013), Columns 6–8 the J-, H-, and K_S-band photometry taken from the 2MASS PSC. Column 9 shows the corresponding NGC 3603 radial angular and projected linear distance (parsecs—assuming a heliocentric distance of 7.6 kpc; Crowther et al. 2010) center distances, and Column 10 the observed wavelength ranges. Finally, in Column 11 we list the IDs of the sources found in the literature, as well as the objects with (when available) X-ray band measurements. The previously assigned IDs for some of the sources listed here (like RFS1, RFS2, RFS3, and RFS4) are from the work of Melnick et al. (1989), while WR42e was previously named by Roman-Lopes (2013b). Also the information on the X-ray source counterparts are from the catalog of Romano et al. (2008) (for RFS1 to RFS5), and in case of RFS10, from the *XMM-Newton* Serendipitous Source Catalog (*XMM-Newton* Survey Science Centre 2013).
[a] Previous spectral type for MTT31 (RFS1) as presented by Moffat et al. (2002).

Figure 1. A colorized *Spitzer* image (blue—3.6 μm, green—4.5 μm, red—8.0 μm) in the direction of the NGC 3603 complex, in which we indicate the position of each source in our sample (shown by labels and arrows), as well as their relative positions to NGC 3603, NGC 3576, and NGC 3590. North is to the top and east to the left. The approximate tidal radius (about 15 arcmin) area is indicated by the blue dotted line.

S/N ≈ 100 (at ≈4800 Å) for a science target with $V = 14 - 15$ (using Goodman at SOAR during graytime night) is about 1.0–1.5 hr, while if we consider the K_S-band magnitude range as defined in Section 2, the necessary average exposure time with OSIRIS at SOAR (to obtain a S/N ≈ 100 in the K_S-band) drops to no more than 15–20 minutes.

3.1. OSIRIS NIR and Goodman Blue-optical Spectroscopic Data Set

The NIR spectroscopic data were obtained by observing runs (summarized in Table 3) during nights that in general presented good weather conditions. The raw frames were reduced following standard NIR reduction procedures, which are

Table 3
Summary of the SOAR Spectroscopic Data Used in this Work

Night	UT	Seeing (″)	Instrument	Mode	Slit	Resolving Power	Coverage
2011 May 09	04:10:00–04:22:00	0.8–1.0	OSIRIS	XD-f/3	1″	1000	1.25–2.35 μm
2011 Dec 18	07:22:00–09:13:00	0.8–1.0	OSIRIS	XD-f/3	1″	1000	1.25–2.35 μm
2012 Jan 31	06:06:00–08:25:00	0.8–1.0	OSIRIS	XD-f/3	1″	1000	1.25–2.35 μm
2012 Dec 29	06:02:00–06:58:00	0.6–0.8	OSIRIS	XD-f/3	1″	1000	1.25–2.35 μm
2013 Jan 26	02:55:00–07:06:00	1.0–1.5	OSIRIS	XD-f/3	1″	1000	1.25–2.35 μm
2013 Feb 28	08:22:00–09:09:00	1.0–1.2	Goodman	GG385-600 1/mm	1.″03	1800	0.45–0.67 μm
2013 Mar 30	07:05:00–07:46:00	0.6–0.8	OSIRIS	XD-f/3	1″	1000	1.25–2.35 μm
2015 Mar 08	04:54:00–08:05:00	1.0–1.5	Goodman	930-m2	1.″03	2100	0.39–0.55 μm
2015 Mar 28	02:15:00–05:16:00	1.0–1.5	Goodman	930-m2	1.″03	2100	0.39–0.55 μm
2015 Jun 29	22:48:00–03:08:00	0.8–1.3	Goodman	930-m2	1.″03	2100	0.39–0.55 μm

presented in detail in Roman-Lopes (2009) and briefly described here. The two-dimensional frames were sky-subtracted for each pair of images taken at two nod positions, followed by division of the resultant image by a master flat. The multiple exposures were combined, and this was followed by one-dimensional extraction of the spectra. Thereafter, wavelength calibration was applied using the sky lines and, being conservative, we estimate as ∼12–16 Å, the 1-σ error for such calibrations. This result comes from the fact that we considered the associated 1-σ error as the mean values measured from the full width half maximum (FWHM) of the sky lines detected in all three NIR bands. On the other hand, if we instead assume the most common criterion of 1/3 of the observed FWHM, then the associated 1-σ error drops to ∼4–5 Å. Also, the effects of the Earth's atmosphere in the science spectra were corrected using *J*-, *H*-, and *K*-band spectra of A-type stars, with the intrinsic hydrogen lines being carefully subtracted by modeling the observed line profiles through the use of Voigt profiles given by the SPLOT task on IRAF.[4] The final NIR spectra were normalized through fitting to the continuum emission observed in the associated wavelength range. We note that, with the exception of RFS2, all the sources in Table 2 were observed in the blue-optical window in 2015 March, with the data acquired using the 1.″03 long slit and the 930-m2 (3850–5550 Å) grating, which provides a maximum resolving power of $R \sim 2100$. On the other hand, RFS2 was observed using Goodman in 2013 February using the GG385-600 1/mm grating with the same slit, a setup that provides a maximum resolving power of $R \sim 1800$, and a wavelength coverage of 4500–6700 Å.

A summary of the SOAR–Goodman observations is shown in Table 3. The reduction of the optical spectra was performed using standard techniques through the use of the packages (alongside others) ONEDSPEC, TWODSPEC, and APEXTRACT within IRAF. The one-dimensional spectra of the science targets were extracted from the two-dimensional frames by summing pixels in the data range and subtracting off the background value for each column, with the background for each column being measured as the median of non-target pixels for each column. Cosmic rays and other anomalous signal detections were suppressed from each of the extracted spectra by removing pixels that deviated 5-σ of the mean within a 100 pixel wide box that steps through the spectrum. The bad pixels were replaced through a linear interpolation of the removed data range, and the wavelength calibration was performed using Hg(Ar) + Ne lamp spectra. As was done in the case of the NIR spectroscopic observations, the final optical spectra were also normalized through the fitting of the continuum emission in the associated wavelength range.

[4] http://iraf.noao.edu/

4. RESULTS AND DISCUSSION

In Figures 2 and 3, we show the OSIRIS and Goodman normalized spectra of the sources in Table 2, with the exception of RFS10 for which we only have the Goodman optical spectrum. The main NIR and optical spectral features are labeled by numbers, with the corresponding transitions being presented in the captions of the figures. As a complement, we also include the NIR and optical spectra of HD 93129A, the prototype of the O2If* class, and until recently, the unique known Galactic exemplar of this extreme O-type star with a published blue-optical spectrum.

4.1. Spectral Types

4.1.1. Three New Galactic Exemplars of the OIf*/WN Intermediate Type Confirmed

The intermediate spectral type OIf*/WN was introduced about three decades ago by Walborn (1982) to classify the emission line star Sk-67 22 in the LMC, and shows spectral features between those of HD 93129A (O2If*) and WR20b (WN6ha). The OIf*/WN type can be separated from the OIf* and WNh types by the P-Cygni morphology of the optical Hβ line, since it is seen uniquely in absorption for O stars (including OIf* stars) and purely in emission for WN stars (Crowther & Walborn 2011). From our NIR survey we identified three new Galactic exemplars of this class, RFS2 (MTT58), RFS5 (WR42e), and RFS7. As can be seen in Figure 2, their NIR spectrograms are characterized by the presence of strong Paβ, Brγ, and He II emission lines. On the other hand, from the optical spectra shown in Figure 3, we note that they all (apart from RFS2 whose optical spectrum did not cover this wavelength range) present strong N IV λ4058 lines in emission, with all three also having powerful He II λ4686 emission lines, as well as Hβ lines showing P-Cygni profiles. Individual comments on the three new OIf*/WN Galactic stars are given as follows.

RFS5. As can be seen in Figure 3, RFS5 has a N IV λ4058 line intensity similar to those of the N III $\lambda\lambda$4604–4620 lines and, taking into account the He II λ4686 line purely in emission, an O3If* supergiant type is assigned. Based on the observed Hβ P-Cygni line profile, and following the criteria presented by Crowther & Walborn (2011), we are now able to

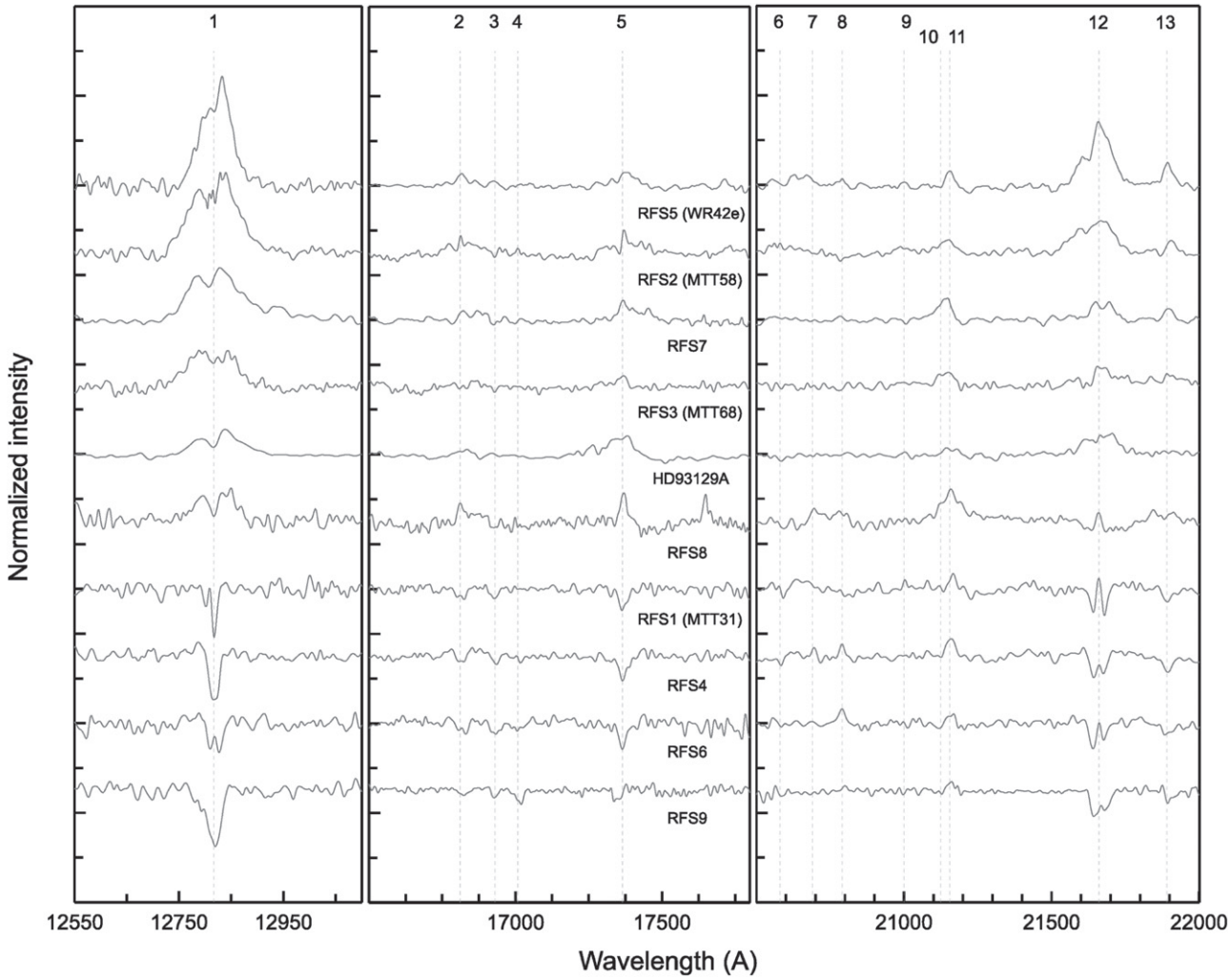

Figure 2. OSIRIS spectra of the sources in Table 2. The main line features are indicated as follow: (1) Paβ λ12822, (2) Br11 λ16811, (3) He II λ16930, (4) He I λ17007, (5) Br10 λ17367, (6) He I λ20590, (7–8) C IV $\lambda\lambda$20690–20802, (9) N V λ21000, (10) He I λ21126, (11) N III λ21160, (12) Brγ, and (13) He II λ21890.

refine the classification of this source by assigning it the O3If*/WN6 type.

RFS2. From RFS2's spectrograms shown in Figures 2 and 3, we can see that they closely resemble those of RFS5. The P-Cygni profile in the Hβ line is also evident, confirming the previous classification based on NIR data made by Roman-Lopes (2013a), who classified it as a star of the OIf*/WN (O2If*/WN6) intermediate type. From the new optical data, it is now possible to improve this classification. Indeed, from the comparison of the strengths of the N III $\lambda\lambda$4604–4620 lines of both stars, which are much weaker in RFS2's spectrogram than those seen in RFS5, we assign an O2If*/WN5 spectral type to this star.

RFS7. From Figure 2, we can see that RFS7 presents NIR spectral features similar to those seen in the spectrograms of RFS3. Indeed, the intensity (and morphology) of the Paβ and Brγ lines are quite similar. However, one also can see that the He II λ21890 line appears much stronger in the *K*-band spectrum of RFS7, a characteristic also noticeable in the *K*-band spectra of RFS2 and RFS5, which, combined with the Paβ broad emission line morphology, may be useful as complementary criteria when discriminating between the two types using solely NIR spectrograms. In this sense, the P-Cygni profile seen in RFS7's Hβ line indicates that this star is a new Galactic exemplar of the OIf*/WN type. As a comment on this, the diffuse interstellar band (DIB) seen at λ4882 appears relatively weak when compared with those present in the RFS5, RFS2, and RFS3 optical spectrograms. Curiously, the other strong DIBs observed at λ4429 are all more or less of the same intensity, which might indicate that its P-Cygni profile should seem stronger than the one observed. According to this, the observed line profile would be the result of the combination of two features: a relatively intense Hβ P-Cygni profile suppressed by a strong and broad DIB absorption line at λ4882. Finally, the N IV λ4058 emission line is stronger than the N III $\lambda\lambda$4604–4620 lines, indicating an intermediate type between O2If*–O3If* (Crowther & Walborn 2011), so we classify RFS7 as an O2.5If*/WN6 star.

4.1.2. RFS1—The First Galactic Exemplar of the O2V Class Identified to Date

The NIR spectra of RFS1 (MTT31—presented in Figure 2), are characterized by the presence of weak Paβ, and Brγ hydrogen recombination lines, which have peculiar absorption +emission profiles (probably indicative of the presence of an intense stellar wind), similar to the one observed in the *K*-band spectrum of Cyg OB2 #7 (Hanson et al. 2006). Also, from a

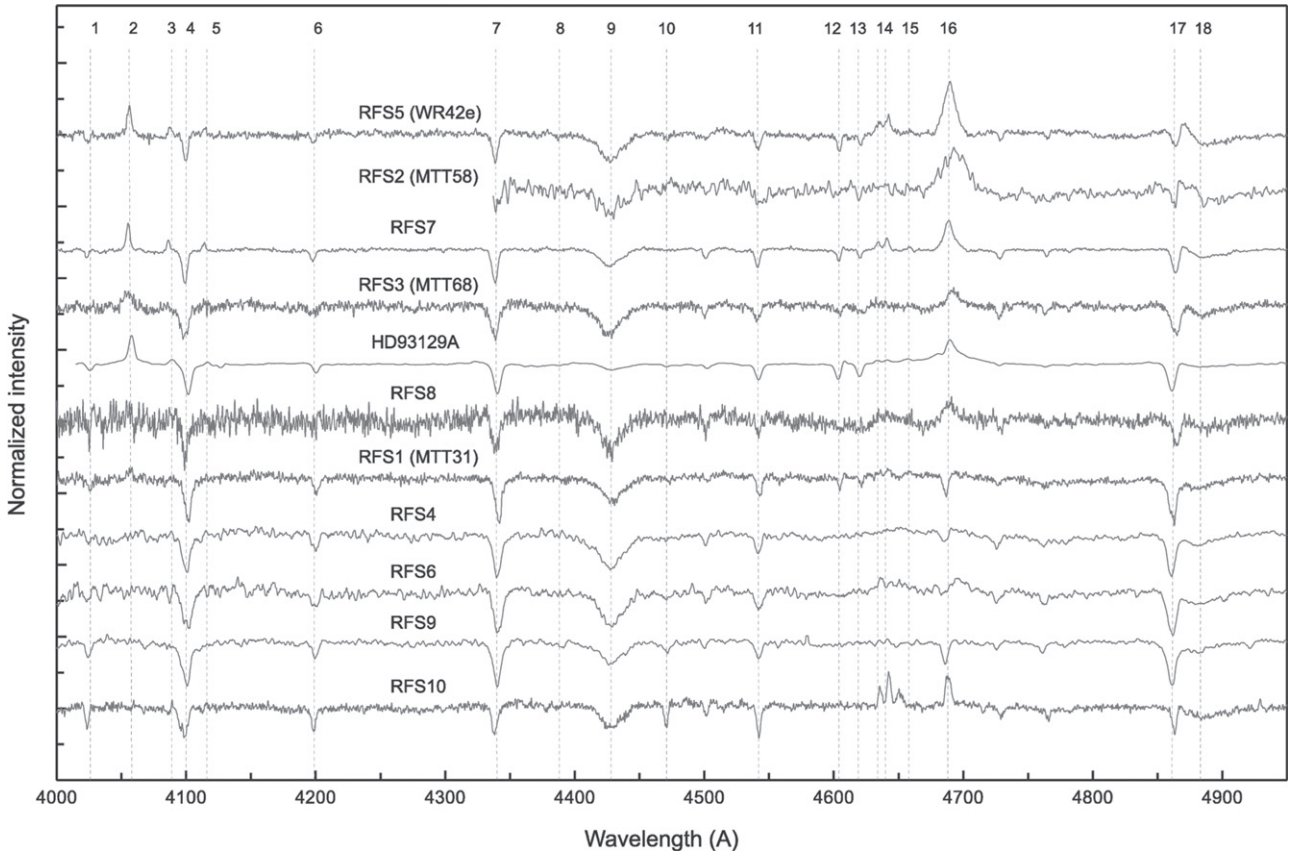

Figure 3. Goodman spectra of the sources in Table 2. The main line features are indicated as follow (Walborn et al. 2002): (1) He I+II λ4026, (2) N V λ4058, (3) Si IV λ4089, (4) Hδ, (5) Si IV λ4116, (6) He II λ4200, (7) Hγ, (8) He I λ4387, (9) DIB λ4429, (10) He I λ4471, (11) He II λ4541, (12–13) N V $\lambda\lambda$4604–4620, (14) N III $\lambda\lambda$4634–4642, (15) C IV λ4658, (16) He II λ4686, (17) Hβ λ4861, and (18) DIB λ4882.

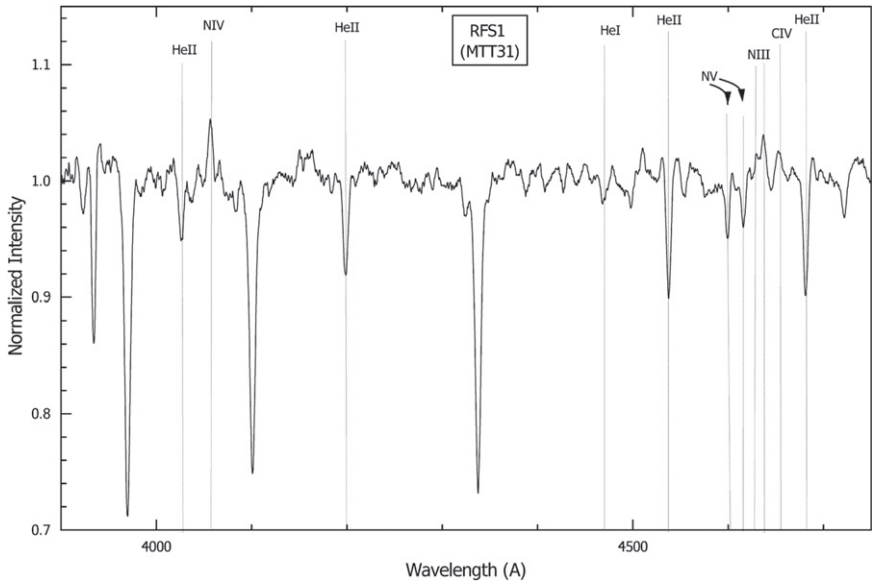

Figure 4. Goodman spectrum of the RFS1 source. The main line features are indicated as follow (Walborn et al. 2002): (1) He I+II λ4026, (2) N V λ4058, (3) He II λ4200, (4) He I λ4471, (5) He II λ4541, (6) N V $\lambda\lambda$4604–4620, (7) N III $\lambda\lambda$4634–4642, (8) C IV λ4658, and (9) He II λ4686.

careful inspection of the $\lambda\lambda$20600–21200 spectral range, one can see the existence of the C IV λ20802 line in absorption together with the N V λ21000 line in emission, features normally only seen in *K*-band spectrograms of stars as early as HD 64568 (O3 v((f))) and Cyg OB2 #7 (O3If*). Moving to the *H*-band, we note that the He I λ17007 line is absent in RFS1's spectrum. However, it does show a strong He II λ16930 line in absorption, as well as the He II λ21890 line in the *K*-band, indicating that RFS1 is a very hot star, probably earlier than O3.

Figure 3 shows the Goodman blue-optical spectrum of RFS1 and, in order to allow a better analysis of it, Figure 4 presents

its individual spectrum in a more detailed and useful way. In particular, the weak lines close to the He II λ4686 line are more visible in this version of the spectrum. The N IV λ4058 line is seen in emission, and the strong He II absorption line at 4200 Å confirms the impression from our above discussion, i.e., that RFS1 is a very hot O-type star. In fact, the N IV λ4058 and N III $\lambda\lambda$4634–4642 emission lines provide strong support to this idea. Finally, the C IV λ4658 line clearly detected in emission led us to classify RFS1 as a new O2v star (Walborn et al. 2002). Indeed, based on a careful inspection of the blue-optical spectrum of BI 253 (the prototype of the O2v class; Walborn et al. 2002) shown in Figure 12(a) of Massey et al. (2005), we can see that the RFS1 blue-optical spectrum is nearly a clone of it, which makes this star the first know Galactic exemplar of the O2v type (Sota et al. 2014).

On the other hand, the detection of what is probably a very weak He I λ4471 absorption line may suggests the presence of a later O-type companion. From a search in the literature, we found that RFS1 has an associated X-ray point source only 0.″16 from its coordinates, cataloged as CXOU111506.69–611633.4 (Townsley et al. 2014). However, the observed X-ray to bolometric luminosity ratio ($\sim 3 \times 10^{-8}$) is found to be compatible with what is expected in the case of a single star ($L_X/L_\odot \sim 10^{-7}$). Further photometric and spectroscopic monitoring studies are necessary in order to test this assumption.

4.1.3. RFS3 Confirmed as a New Galactic O2If* Star

RFS3 (MTT68) was first cataloged as a probable member of NGC 3603 by Melnick et al. (1989), and discovered to be a strong *Chandra* point source by Moffat et al. (2002), who performed an extensive X-ray–radio study of the 3.′6 × 3.′6 field centered on NGC 3603. Later, based on *J*-, *H*-, and *K*-band SOAR–OSIRIS spectra, it was classified as an O2If* star by Roman-Lopes (2013a), who found its NIR spectra to be very similar to those of HD 93129A, the template of the class (Walborn et al. 2002) and, at that time, the only known Galactic O2If*. Based on our new Goodman blue-optical spectra of RFS3 (shown in Figure 3), we may now confirm that this object is indeed a highly reddened O2If* star, as indicated by the strong DIBs seen at ∼4430 Å and 4480 Å. As previously noted by Roman-Lopes (2013a) in the NIR, the RFS3 optical spectrum also looks quite similar to that of HD 93129A, as indicated by the intense N IV λ4058 emission line, which is much stronger than the N III emission line pair at $\lambda\lambda$4634–4642. Combined with the strong He II λ4686 emission line (Crowther & Walborn 2011), this confirms its O2If* nature. However, from a careful inspection of the NIR emission line features seen in the spectra of both stars (e.g., the Paβ and the N III λ21150 lines), we can see that the observed emission lines appear broader in the RFS3 NIR spectrograms, a characteristic that is also quite evident in the N IV λ4058 optical line, which may suggest the existence of a secondary companion of RFS3, which in this case should also be another extreme early-type star.

4.1.4. New Early- and Mid-O Galactic Supergiants

In addition to the O2If* and OIf*/WN stars discussed above, there are two other sources in Table 2 (RFS8 and RFS10) that show the He II λ4686 line in emission. Unfortunately, due to a problem during the acquisition process, the NIR spectra of RFS10 were not useful for spectral analyses, so in this case our main conclusions only rely on optical data. In what follows, we discuss in some detail the results obtained for these two objects.

RFS8. The NIR spectrograms of the RFS8 source (shown in Figure 2), are dominated by emission line features associated with the Paβ, Brγ, Br10, and Br11 hydrogen atomic transitions, as well as by broad emission line profiles corresponding to the C IV $\lambda\lambda$20690–20802 and N III λ21160 transitions. The morphology of the Paβ emission line is quite similar (in terms of both shape and intensity) to the one seen in the *J*-band spectrum of HD 93129A, however, the Brγ line profile is completely different. Also, the He II lines λ16930 and λ21890 appear in absorption, suggesting a later spectral type. The blue-optical spectrum for this source (shown in Figure 3) confirms this assumption. The intense emission feature associated with He II λ4686 indicates a supergiant status for this object. Also, the N IV λ4058 emission line is seen as less intense than those of the N III $\lambda\lambda$4634–4642 pair, which, combined with the fact that the N V $\lambda\lambda$4604–4620 lines appear weaker than those seen in the HD 93129A blue-optical spectrogram, indicate a spectral type later than O3. Finally, the absence of a He I λ4471 absorption line suggests a spectral type probably no later than O4–O4.5 (Sota et al. 2011). Taking into account the points discussed above, and the criteria presented by Crowther & Walborn (2011), we assign an O3.5If* spectral type to the RFS8 source.

RFS10. As mentioned above, for this star we only have optical data, and its spectrogram is shown in Figure 3. It is a high S/N optical spectrum in which the He II λ4686 emission line denotes a supergiant class for this source. The absence of N V $\lambda\lambda$4604–4620 lines associated with the presence of a strong He I λ4471 absorption line indicate that this star is of a spectral type later than O3.5–O4 (Sota et al. 2011). Also, from the library of optical spectra of O-stars of Sota et al. (2011), one can see that the relative intensities of the two N III $\lambda\lambda$4634–4642 emission lines and the He I λ4471 and He II λ4541 absorption lines make this spectrum quite similar to that of HD 169582, the standard of the O6Ia type. We searched the literature for X-ray sources associated with RFS10, and found a strong one in the *XMM-Newton* catalog only 0.″35 from RFS10's coordinates, identified as J111955.1–611603. Further photometric and spectroscopic studies are required for this source, as the detected X-ray emission could be due to the presence of a close binary companion.

4.1.5. Early-O-Type Stars

The sources in this group are RFS4, RFS6, and RFS9, whose spectral features are typical of early and mid-O-type stars. In the following, we discuss each object in detail.

RFS4 (MTT71). The *J*-, *H*-, and *K*-band spectra of RFS4 (presented in Figure 2) are very similar to those of RFS1, with a small but remarkable difference: the presence of the He I λ17007 absorption line which, however, is less intense than the He II λ16930 line. This feature indicates that this source is also an early-O-type star, and from a comparison with the *H*-band spectra of HD 46223 (O4v), HD 66811 (O4 I), HD 14947 (O5 If), and Cyg OB2 8c (O5 If) (Hanson et al. 2006), one can see that the *H*- and *K*-band features of RFS4 are compatible with those seen in O-type stars of spectral types O4–O5. On the other hand, the Goodman normalized spectrum of RFS4 (shown in Figure 3) does not show the He I λ4471 absorption line, so an early-O-type status for this star is confirmed. Also, the absence of a N IV λ4058 line (in emission or absorption)

indicates that this star is of a spectral type not earlier than O4. Indeed, the optical spectrum of HD 168076AB (O4III) is virtually a clone of the RFS4 Goodman spectrogram, including the incipient P-Cygni profile seen in its He II λ4686 line, allowing us to classify RFS4 as a new Galactic O4III star. As a final comment on this source, from a cross-check with X-ray catalogs in the literature, we found a point source (only 0.″05 from the star) cataloged as CXOU111521.31–611504.3 (Townsley et al. 2014). Indeed, RFS4 was first discovered as a strong X-ray point source by Moffat et al. (2002) who suggested that it could be due to colliding wind binary interaction, which may suggest the existence of an early-O-type companion. Further studies are necessary in order to properly address this assumption.

RFS6. The OSIRIS and Goodman spectra for this source look quite similar to those of the RFS4 source. Indeed, the presence of strong He II $\lambda\lambda$16930–21890 absorption lines and the weakness of He I λ17007 transition, combined with the absence of the He I absorption line λ21130, give support to this idea. Also, taking into account the presence of strong C IV and N III $\lambda\lambda$20800–21160 emission lines led us to the conclusion that this star is probably another exemplar of the early-type O-star family. In support of this, the optical spectrogram shown in Figure 3 also looks quite similar to that of RFS4, except for the He I λ4471 line which is clearly seen (weakly) in absorption, which is not uncommon for O4–O5 stars like HD 46223 (O4V), HD 66811 (O4I), HD 14947 (O5If), and Cyg OB2 8c (O5If) (Hanson et al. 2006).

RFS9. The NIR spectrograms of the RFS9 source are shown in Figure 2. As can be seen, its *J*-band spectrum presents a strong and broad Paβ absorption line, a feature also noted in the profiles of the *H*- and *K*-band Bracket lines. The He II lines at λ16930 and λ21890 are also seen in absorption, and there is no sign of the He I line at 21113 Å, so a spectral type later than O6V is ruled out (Hanson et al. 2006). On the other hand, the He I absorption line λ17007 is stronger than He II λ16930, an indication that this star is possibly of a type later than O4. From the optical spectrogram of the RFS9 source, shown in Figure 3, we can see that the He II λ4686 line is seen purely in absorption, so a dwarf class is assigned. Based on the above discussion, we performed a careful examination of the O4V–O5V optical spectra presented in the literature, concluding that our Goodman spectrum of the source RFS9 looks quite similar to those of HD 15629 (O4.5V), HD 46150 (O5V), and HD 93204 (O5V), presented in Sota et al. (2011), and that of source #108 (O5.5V) of Melena et al. (2008). An interesting spectral characteristic that caught our attention is the He II $\lambda\lambda$4686 absorption line, which is stronger than any other He II lines present in the $\lambda\lambda$4000–5000 wavelength range. Such an O-type spectral feature is believed to be characteristic of the Vz class. It seems that the Of effect (established as a luminosity indicator in normal O-type spectra) is suppressed by the Vz effect, generating less emission than in normal class V spectra, which might indicate extreme stellar youth (Walborn et al. 2014).

A natural question that arises from this result is, how can such an extremely young O-star be found at such a large angular distance from the NGC 3603 cluster center? A possible answer is that RFS9 belongs to an independent star-forming complex embedded in the main body of the NGC 3603 complex. In an upcoming paper (Roman-Lopes et al. in preparation), we further discuss the issue of how many of the sources in Table 2 could have arrived at their present locations.

4.2. Interstellar Extinction, Absolute Magnitudes, Ages, and Masses

4.2.1. Interstellar Extinction

The interstellar extinction law in the direction of NGC 3603 appears to be anomalous. This is not surprising, as it is well known that very young H II regions in general show ratios of total to selective extinction values well above the canonical value $R_V = 3.1$ (Chini & Kruegel 1983; Chini & Wargau 1990). Pandey et al. (2000) performed an extensive *UBVRI* CCD photometric survey in the direction of the innermost region (2.′08 × 3.′33 FOV) of the cluster, and from a variable extinction analysis of the sources with color excess in the range $1.30 < E(B-V) < 1.75$, they computed a mean value for the total to selective extinction ratio $R_V = 3.8 \pm 0.8$. The large uncertainty on the mean reflects the large scatter on the individual derived values. Also, by following the method of Neckel & Chini (1981) they were able to obtain the intra-cluster total to selective extinction ratio value $R_V = 4.1 \pm 0.2$.

In Table 4, in addition to the spectral types and effective temperatures, we present the $(B-V)$ colors for each star in our sample, together with the associated optical to NIR color excesses $E(B-V)$, $E(J-V)$, $E(H-V)$, and $E(K-V)$, which were derived using the intrinsic colors for the earliest O-stars given by Martins & Plez (2006). The values of the total to selective extinction ratio were then estimated using the equations A3–A6 of Fitzpatrick (1999) and, by using R_V and $E(B-V)$, we computed the corresponding extinction parameter A_V for each star in Table 2. From the R_V values in Table 4, we can see that for most of the stars in our sample the associated interstellar law is in agreement with the previous study of Pandey et al. (2000), with R_V ranging from 3.19 for RFS9 to 4.24 in case of RFS2, with a mean value (error of the mean $\sigma/\sqrt{n}$, with n being the number of stars in our sample) of $R_V = 3.73 \pm 0.35$. As in previous studies, the relatively large error value on the mean probably reflects the moderate scatter in the computed ratio of total to selective extinction in the direction of NGC 3603, which in turn is probably produced by variations in dust and gas column densities, and perhaps by differences in dust composition and grain size.

In Figure 5, we plot the parameter R_V as a function of the cluster center distance r_c for the sources in Table 4. We can see that with the exception of RFS8, the associated R_V values decrease as a function of r_c. In the same plot we also present the results of linear fittings considering all sources in the sample, as well as only those (six) presenting r_c values less than the NGC 3603 cluster tidal radius estimated by Sung & Bessell (2004). The resulting linear equations correlating R_V and r_c are $R_V = 3.881 - 0.014 r_c$ and $R_V = 3.919 - 0.026 r_c$, for the entire sample and only for those sources inside the NGC 3603 tidal radius area, respectively. The values of R_V computed from our fittings limited to the radial cluster center distance of 2 arcmin are $R_V = 3.85$ and $R_V = 3.87$, respectively, in good agreement with the result obtained by Pandey et al. (2000). Finally, from the extinction parameters presented in Table 4, we computed mean values and uncertainties (errors on the mean) of the ratios A_λ/A_V for the *J*-, *H*-, and K_S-bands, obtaining $A_J/A_V = 0.286 \pm 0.004$, $A_H/A_V = 0.170 \pm 0.003$, and $A_{Ks}/A_V = 0.098 \pm 0.005$.

4.2.2. Absolute Magnitudes, Ages, and Masses

The absolute magnitudes for the sources in Table 4 were derived using the observed magnitudes and associated

Table 4
Spectral Types, Absolute Magnitudes, and Extinction Law Parameters Obtained for the Sources in Table 2.

Source	SpType	Log Teff	$(B-V)$	$E(B-V)$	$E(J-V)$	$E(H-V)$	$E(K-V)$	R_V	A_V	M_V	M_J	M_H	M_K	A_J	A_H	A_K
RFS1	O2V	4.67	1.22	1.50	−4.07	−4.69	−5.09	3.78	5.67	−6.00	−5.33	−5.21	−5.12	1.60	0.98	0.58
RFS2	O2If*/WN5	4.64	1.38	1.66	−4.96	−5.87	−6.40	4.24	7.04	−6.68	−6.01	−5.89	−5.80	2.08	1.17	0.64
RFS3	O2If*	4.64	1.59	1.87	−5.41	−6.34	−6.86	4.07	7.61	−7.29	−6.62	−6.50	−6.41	2.20	1.27	0.75
RFS4	O4 III	4.63	1.57	1.85	−4.81	−5.54	−6.02	3.62	6.70	−6.36	−5.69	−5.57	−5.48	1.89	1.16	0.68
RFS5	O3 If*/WN6	4.64	1.52	1.80	−5.02	−5.85	−6.37	3.92	7.05	−6.92	−6.25	−6.13	−6.04	2.03	1.20	0.68
RFS6	O4.5 V	4.62	1.50	1.78	−4.55	−5.25	−5.67	3.56	6.33	−6.22	−5.55	−5.43	−5.34	1.78	1.08	0.66
RFS7	O2.5If*/WN6	4.64	1.28	1.56	−3.71	−4.29	−4.65	3.32	5.18	−6.69	−6.02	−5.90	−5.81	1.47	0.89	0.53
RFS8	O3.5If*	4.61	1.32	1.60	−4.74	−5.55	−6.08	4.18	6.69	−6.41	−5.74	−5.62	−5.63	1.95	1.14	0.61
RFS9	O5Vz	4.61	1.36	1.64	−3.74	−4.35	−4.67	3.19	5.22	−5.85	−5.18	−5.06	−4.97	1.48	0.87	0.55
RFS10	O6Ia	4.56	1.35	1.63	−3.99	−4.62	−5.08	3.44	5.60	−6.14	−5.47	−5.35	−5.26	1.61	0.98	0.52

Note. Column 1: ID. Columns 2–6: colors and associated optical to NIR color excesses. The color excesses were calculated using the corresponding $(B-V)_0$, $(J-V)_0$, $(H-V)_0$, and $(K-V)_0$ intrinsic colors taken from Martins & Plez (2006). Column 7: the total to selective extinction ratio R_V values were derived using Equations A3–A6 of Fitzpatrick (1999). Column 8: visual extinction computed from $E(B-V)$ and R_V. Column 9: absolute visual magnitudes M_V obtained using A_V plus the visual magnitudes for each source in Table 2, applied in the distance modulus equation for an heliocentric distance of 7.6 ± 0.35 kpc (Crowther et al. 2010). Columns 10–12: the same for the M_J, M_H, and M_K absolute magnitudes, using the $V-J$, $V-H$, and $V-K$ color values taken from Martins & Plez (2006). Columns 13–15: A_J, A_H, and A_K extinction values derived using the *J*-, *H*-, and *K*-band magnitudes from Table 2, together with the associated M_J, M_H, and M_K values applied into the distance modulus equation.

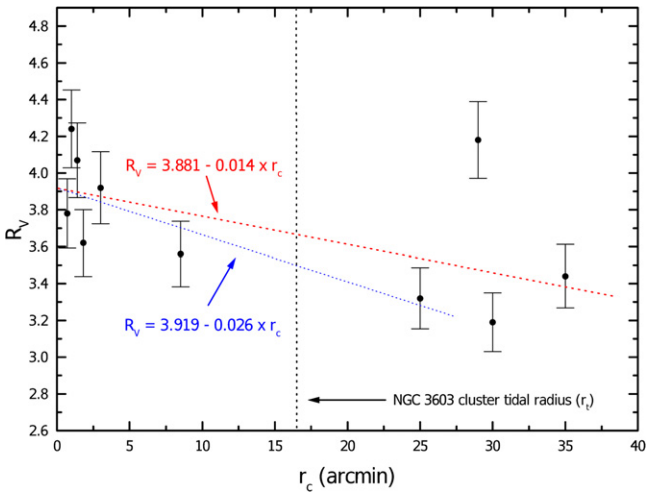

Figure 5. R_V as a function of the cluster center radius r_c for the sources in Table 4. We can see that with the exception of RFS8, the associated R_V values decrease approximately linearly as a function of r_c. In the same plot we also present the results of linear fittings considering all sources in the sample, as well as those (six) presenting r_c values less than the NGC 3603 cluster tidal radius estimated by Sung & Bessell (2004).

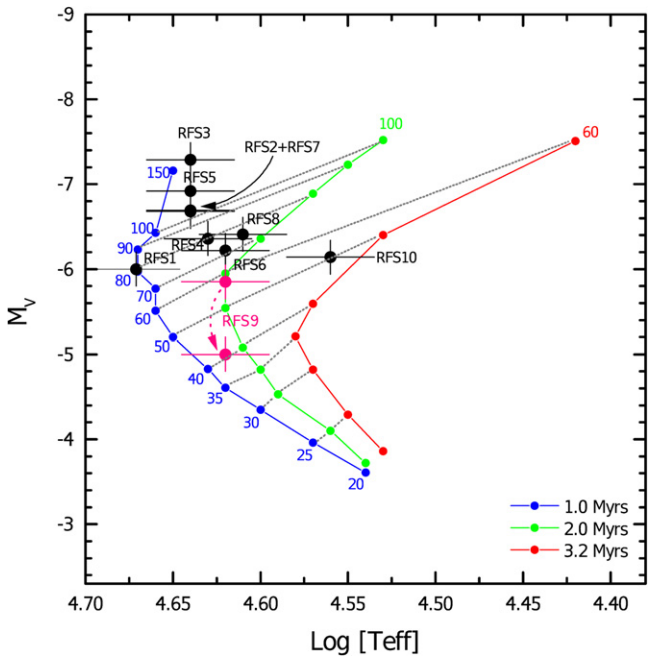

Figure 6. The M_V vs. Log T ($T_{\rm eff}$) H–R diagram for the sources in Table 4. The effective temperatures for the O I, O III, and O V classes were computed using Equation (2) presented in the work of Martins et al. (2005), while the values for the OIf*/WN stars were estimated from the work of Crowther et al. (2010). For all sources we assumed an uncertainty of ±3000 K on the quoted temperature values. We also present the 1, 2, and 3.2 Myr isochrons (see Footnote 5) taken from the work of Bressan et al. (2012), for stars with initial masses in the range 20–150$M_\odot$(solar metallicity $Z = 0.015$). RFS9 is represented considering single and binary systems comprising two stars of the same spectral type. In this sense, assuming a mean absolute visual magnitude $M_V = -5.0$ for each component would result in a combined absolute magnitude $M_V = -5.8$, a value in line with the one derived by us (considering the associated uncertainties) using the distance modulus equation, equivalent to a binary system comprising two stars of 40 $M_\odot$ each (see the text in Section 4.2.2).

extinction values applied in the distance modulus equation, adopting an heliocentric distance of 7.6 ± 0.35 kpc (Crowther et al. 2010). Also, the respective M_J, M_H, and M_K absolute magnitudes were calculated using the $(V-J)_0$, $(V-H)_0$, and $(V-K)_0$ intrinsic colors for early-O stars taken from Martins & Plez (2006). In Figure 6, taken from the work of Bressan et al. (2012), we present the M_V versus Log T ($T_{\rm eff}$) Hertzprung–Russel (H–R) diagram for sources in Table 4. The effective temperatures for the O I, O III, and O V classes were obtained using Equation (2) presented in the work of Martins et al. (2005), while the values for the OIf*/WN stars were estimated from the work of Crowther et al. (2010). For all sources we assumed an uncertainty of ±3000 K on the quoted values. We also present the 1, 2, and 3.2 Myr isochrons[5] taken from the work of Bressan et al. (2012), for stars with initial masses in the range 20–150$M_\odot$(solar metallicity $Z = 0.015$).

From this diagram we can see that the youngest sources are RFS1, RFS2, RFS3, RFS5, and RFS7 with probable ages of about 1 Myr. The new O2If* star (RFS3) with initial mass above 150 $M_\odot$, appears as the most massive and luminous object of our sample. This is not surprising as O2If* stars are known to belong to the most massive and luminous type of O-stars in the local universe. For example, HD 93129A, the most massive and luminous O-star previously known in the Galaxy, has an absolute visual magnitude $M_V = -6.6$ (Simon et al. 1983) and an estimated initial mass of 130 ± 15 $M_\odot$ (Taresch et al. 1997). On the other hand, in the LMC we have the extreme case of Mk42, an O2If* star presenting an absolute visual magnitude $M_V = -7.4$, and an initial mass of 189 $M_\odot$ (Bestenlehner et al. 2014).

Accordingly, with the isochrons shown in Figure 6, all three new Galactic OIf*/WN stars had initial masses well above 100 $M_\odot$, with RFS5 (O3If*/WN6) being a bit more massive than RFS2 and RFS7. Placed in the same star-forming complex, NGC 3603-C has the same spectral type (O3If*/WN6), with $M_V = -7.2$ and an estimated initial mass in the range 123–154 $M_\odot$ (Crowther et al. 2010). Taking into account the evolutionary models and RFS5's position in the *H–R* diagram of Figure 5, we can conclude that for an estimated age of 1 Myr, RFS5 should have initial and current masses of 135 $M_\odot$ and 123 $M_\odot$, respectively, a result in line with those obtained by Crowther et al. (2010) in their analyses of NGC 3603-C. In addition to the three new OIf*/WN stars, another very young star in our sample is RFS1. From its position in the *H–R* diagram of Figure 6, we can see that it is an O2V star with probable initial and current masses of 80 $M_\odot$ and 76 $M_\odot$, respectively. As the only Galactic star of its class known to date, RFS1 has an absolute magnitude of $M_V = -6.0$, corresponding to a luminosity similar to other O2V stars found in the LMC, like VFTS 621 (O2V) and VFTS 512 (O2V-III), both presenting visual absolute magnitudes of $M_V = -6.1$ (Bestenlehner et al. 2014).

A second group of slightly older sources, with ages ranging from 1.5–2.0 Myr, comprises RFS4 (O4III), RFS6 (O4.5III), RFS8 (O3.5If*), and RFS9 (O5Vz). From their associated absolute visual magnitudes (Table 4) we can see that they also appear as very luminous sources, and based on the comparison of their values with those from other stars of similar spectral types, we conclude that our results are in line with those found in the literature, with the exception of RFS9, which appears more luminous than expected from the comparison with other LMC and Galactic O5Vz stars. We will further discuss this source later.

[5] http://stev.oapd.inaf.it/cgi-bin/cmd

The absolute visual magnitudes of RFS4 and RFS6 are quite consistent with the values for stars of similar spectral types found in the LMC, as for example VFTS 422 (O4III)—$M_V = -5.8$, VFTS 603 (O4III)—$M_V = -6.3$, and VFTS 608 (O4III)—$M_V = -6.0$. On the other hand, in the Milk Way we have the cases of HD 168076 (O4III) with an absolute visual magnitude $M_V = -5.9$ (Sana et al. 2009), HD 93250 AB (O4III) presenting $M_V = -6.2$ with an estimated stellar mass of 83 $M_\odot$(Repolust et al. 2004), as well as in the innermost part of NGC 3603, the source #38 of Melena et al. (2008) (O4III) with $M_V = -6.0$.

The case of RFS8 (O3.5If*) is quite interesting. Indeed, it is located well to the south of the complex, in apparent isolation at the large radial angular center distance of 29′, or equivalently, at a projected linear distance of about 62 pc considering the quoted NGC 3603 heliocentric distance of 7.6 kpc. Based on its location in the *H–R* diagram of Figure 5, and accordingly with the stellar evolutionary models, RFS8 would have initial and current masses of 77 $M_\odot$ and 70 $M_\odot$, respectively. Its derived absolute magnitude $M_V = -6.4$ is similar to that of another O3.5If* (Sh18) found in NGC 3603's innermost region, with an absolute magnitude $M_V = -6.3$ (Bestenlehner et al. 2011). The fact that a such high mass star is found isolated in the field naturally led us to speculate whether it could have been expelled sometime in the past from the innermost parts of the complex. Looking for proper motion measurements for this star, and based on a search in the PPMXL and XPM proper motion catalogs (Roeser et al. 2010; Fedorov et al. 2011), we found that RFS8 has proper motion parameters of pmRA $= -34.3 \pm 11.8$ mas yr^{-1}and pmDE $= -53.2 \pm 11.8$ mas yr^{-1}, and pmRA $= -40.0 \pm 10.0$ mas yr^{-1} and pmDE $= -58.6 \pm 10.0$ mas yr^{-1}, respectively, quite high for an object that is assumed to be placed at the same heliocentric distance of NGC 3603. Indeed, a distance of 7.6 ± 0.35 kpc would result in a projected linear velocity of about 240 km s^{-1}! Despite the fact that such a high velocity for a very high mass star might at first seem unlikely, Gvaramadze & Gualandris (2011) showed from their study on the dynamical ejection scenario of massive runaway stars that such a high mass runaway star could actually exist. Indeed, they argue that the most effective process generating this kind of high velocity star is that produced by a close fly-by dynamical encounter between a single massive star with a very massive hard binary system. For example, in the case of an NGC 3603-A1-like binary system ($M_1 = 120\ M_\odot + M_2 = 90\ M_\odot$), in a few per cent of cases a 60–80 $M_\odot$ M_3 fly-by star would acquire a peculiar velocity as high as 250 km s^{-1}. Further proper motion measurements such as those to be provided by the *Gaia* space astrometry mission, are necessary to give (or not) additional support to this idea.

From RFS9's location in the H–R diagram of Figure 5, we can see that its derived absolute magnitude ($M_V = -5.85$) is not consistent with the absolute visual magnitudes for single stars of the O5vz type in the LMC, such as, for example, VFTS 385 ($M_V = -5.2$, log ($T_{\rm eff}$) = 4.63), VFTS 511 ($M_V = -4.9$, log ($T_{\rm eff}$) = 4.64), and VFTS 581 ($M_V = -5.0$, log ($T_{\rm eff}$) = 4.60) (Sabín-Sanjulián et al. 2014). A possible explanation for this discrepancy can be obtained if we consider the case in which RFS9 is a binary system comprising two stars of the same spectral type. In this sense, assuming a mean absolute visual magnitude $M_V = -5.0$ for each component would result in a combined absolute magnitude $M_V = -5.8$, a value in line with the one derived by us (considering the associated uncertainties) using the distance modulus equation. In this case, from Figure 5 we can see that RFS9 would be a binary system comprising two stars of 40 $M_\odot$ each.

With an estimated age of about 3 Myr (in accord with the isochrons of Bressan et al. 2012), RFS10 appears to be the oldest star in our sample with initial and current masses of 45–55 $M_\odot$ and 40–50 $M_\odot$, respectively. Its derived absolute visual magnitude $M_V = -6.14$ and spectroscopic mass of 45–55 $M_\odot$ agree with the corresponding values obtained for Galactic O5–O6Ia stars ($M_V = -6.1$) (Wegner 2005), as well as with the values of stars of similar spectral type and luminosity class in the LMC, such as VFTS 151 (O6.5II(f)p—$M_V = -6.4$, $M = 79\ M_\odot$), VFTS 208 (O6 (n)fp—$M_V = -5.8$, $M = 53\ M_\odot$), and VFTS 440 (O6-O6.5II(f)—$M_V = -6.2$, $M = 76\ M_\odot$).

4.3. Identifying the OIf*/WN Type Solely from NIR Spectrograms

With the use of new efficient detectors and large ground-based telescopes, the NIR window has become available for spectral typing (Hanson et al. 1996, 2006; Crowther & Walborn 2011, and references therein). This is particularly important when dealing with highly obscured and distant early-type stars. However, despite the observational progress made during the few last years, the number of known Galactic OIf*/WN stars with studies in both the optical and NR domains is relatively small. Considering that the majority (if not all) of the remaining members of the OIf*/WN Galactic stellar population are probably going to be discovered (and properly studied), mainly using NIR spectroscopic facilities, one important question (already posed by Crowther & Walborn 2011) is, can we safely distinguish between the OIf* and OIf/WN types using only NIR spectroscopy? In order to contribute to addressing this question, in the following we will make use of the NIR spectral line measurements taken from our new set of Galactic O, OIf*, and OIf*/WN stars, which were spectroscopically classified using the data collected with OSIRIS and Goodman at SOAR.

In Tables 5 and 6 we present the equivalent width (EW) and line width (LW) measurements taken from the observed NIR and optical lines. As a complement we also present in Table 5 the EW and LW measurements of relevant NIR lines, obtained from a set of unpublished *J*-, *H*-, and *K*-band OSIRIS spectra of WR20a (O3If*WN6+O3If*/WN6), WR20aa (O2If*/WN5), and WR25 (O2.5If*/WN6+O) (Rosslowe & Crowther 2015), taken during previous nights with SOAR. From the associated values, we constructed the EW and EW × LWHM comparative diagrams shown in Figures 7 and 8, respectively, and based on them, one can see that the normal O-type stars (represented by the blue squares), in general, are well separated from the OIf* and OIf*/WN stars. This is particularly true even when considering the spectral lines seen in emission in all NIR spectrograms, such as, for example, the N III $\lambda\lambda$21160 transition (figure 7(b)). On the other hand, the separation of the normal O-type stars from the OIf* and OIf*/WN groups is clearly seen in all other panels of Figure 7.

In the specific case of using only the *K*-band to separate normal O-type stars from the OIf* and OIf*/WN types, the best comparative diagram to use is the one presenting the He II × Brγ EW line measurements, as seen in figure 7(a). In fact, in this case it is possible not only to identify the locus of normal O-type stars, but also to separate the majority of the OIf*/WN

Table 5

EW and NIR LW Measurements (Å), for the Sources in Table 2, with the Exception of RFS10, for which we Only have Optical Data, with the Uncertainty on the Quoted Values Varying from 10%–15%

Source	Paβ (1) EW–LW	Br11 (2) EW–LW	He II (3) EW–LW	He I (4) EW–LW	Br10 (5) EW–LW	C IV (7–8) EW–LW	N V (9) EW–LW	He I (10) EW–LW	N III (11) EW–LW	Brγ (12) EW–LW	He II (13) EW–LW
RFS1	1.3–8.8	0.85–32.5	0.62–21	0–0	1.8–25.9	1.1–54	−0.3–6.9	0–0	−0.88–19.2	em+abs	1.1–27.9
RFS2	−19.4–97.5	−4.2–117	2013;0	0–0	−5.6–172	0.36–21.2	−0.72–35.5	0–0	−1.4–39.8	−15.7–126.7	−2.3–44.5
RFS3	−9.8–102.5	2013;0	2013;0	0–0	−2.5–71.9	2013;0	2013;0	0–0	−2.4–49.3	−4.1–91.4	−2.2–95.2
RFS4	2.4–17.2	1–29.4	0.7–14.4	0.2–8.5	1.9–21.9	−0.74–16.5	2013;0	0–0	−1.6–30.2	3.1–54.2	1.2–25.5
RFS5	−17.7–65.5	−1.3–32.9	−0.59–31.6	0–0	−3.1–67	−0.82–26.9	−0.4–7.3	0–0	−2–25.2	−14.3–65	−2.5–28.5
RFS6	2.0–26.8	1–33.0	1.2–33.9	0.9–40.4	2.4–27.8	−1–24.8	2013;0	0–0	−0.73–25.2	2.5–46.2	1.7–58.9
RFS7	−15.3–105	−2.2–86.4	2013;0	0–0	−4.7–113	2013;0	−0.9–43.9	0–0	−2.8–40.4	−3.2–40.4	−2.3–103
RFS8	−5.4–88.7	−1.9–42	2013;0	0–0	−3.2–36.6	−5.7–128	2013;0	0–0	−7.4–83.4	3.6–114	−1.8–66.1
RFS9	4.7–26.7	0.4–25.9	0.4–15.5	1.1–22.1	0.82–25.5	−0.28–14.7	2013;0	0–0	−0.65–23.8	3.8–58	1–30
HD 93129A	−5.7–99.0	−1–55	2013;0	0–0	−6.2–105	−0.3–24	−0.2–13	0–0	−1.1–57	−6.3–124	2013;0
WR20a	−26.7–85.0	−2.2–65.1	−11.1–175	⋯	−12.1–87.2	⋯	⋯	⋯	−2.2–78.3	−30.5–132	−6.9–91.4
WR20aa	−16.3–71.4	−2.2–57.3	−0.47–30	⋯	−5.3–54.8	⋯	⋯	⋯	−2.5–50	−18.6–129	−6.9–92
WR25	−22.5–70.0	−2.7–53.7	−4.5–87.6	⋯	−8.4–87.6	⋯	⋯	⋯	−3.4–56.8	−32.2–102.4	−12.3–87.6

Table 6

EW and LW Measurements of Selected Optical Lines (Å), for the Sources in Table 2, with the Uncertainty on the Quoted Values Ranging from 10%–15%

Source	He I+II (1) EW–LW	N IV (2) EW–LW	He II (6) EW–LW	He I (10) EW–LW	He II (11) EW–LW	N V (12) EW–LW	N V (13) EW–LW	N III (14-1) EW–LW	N III (14-2) EW–LW	C IV (15) EW–LW	He II (16) EW–LW	Hβ (17) Profile
RFS1	0.34–3	−0.46–4.5	0.57–4.4	0.06–1.02	0.71–4.1	0.23–2.1	0.18–2.5	−0.16–3.6	−0.23–3.8	−0.16–4.7	0.71–4.1	pure abs
RFS2	…	…	…	…	1.5–10.4	0.27–5.1	0.25–2.9	…	…	…	−7.5–20.6	P-Cygni
RFS3	0–0	−1–7.7	0.39–6.7	0–0	0.73–5.4	0.4–6.2	0.47–8.1	−0.2–14.3	0–0	0–0	−1.46–10.7	pure abs
RFS4	0–0	0–0	0.76–5.4	0–0	0.82–4.4	0–0	0–0	0–0	0–0	0–0	0.53–5.3	pure abs
RFS5	0.3–3.3	−1.2–3.6	0.33–3.6	0.14–3.3	0.52–4.4	0.38–3.2	0.26–3.2	−0.58–5.8	−0.72–4.8	0–0	−6.6–16.5	P-Cygni
RFS6	0–0	0–0	0.69–5.3	0.32–6	0.99–6.4	…	…	…	…	…	0.53–5.4	pure abs
RFS7	0.12–2.1	−0.8–2.8	0.34–3.8	0–0	0.56–3.7	0.2–2.3	0.17–2.6	−0.19–2.8	−0.36–3.3	−0.28–4.8	−4.3–12.8	P-Cygni
RFS8	0–0	−0.26–1.5	0.54–6	0–0	0.4–2.8	0.21–6	0.07–1.9	−0.4–6	−1.1–10	−0.7–11.2	−2.2–11.3	pure abs
RFS9	0.58–4.1	0–0	0.6–3.8	0.57–5.9	0.73–5	0–0	0–0	0–0	0–0	0–0	0.86–3.8	pure abs
RFS10	0.47–2.6	0–0	0.8–3.9	0.59–3.2	0.98–3.3	0–0	0–0	−0.41–2.9	−0.88–3.4	0–0	−1.28–4.4	pure abs
HD 93129A	0.28–4.7	−1.5–5.5	0.35–4.6	0.13–5.8	0.8–4.7	0.7–4	0.67–4.7	−0.1–4.2	−0.09–4.5	−0.09–5.4	−4.2–24	pure abs

Note. We also show the values for HD 93129A taken from the optical spectrum in Roman-Lopes et al. (2011).

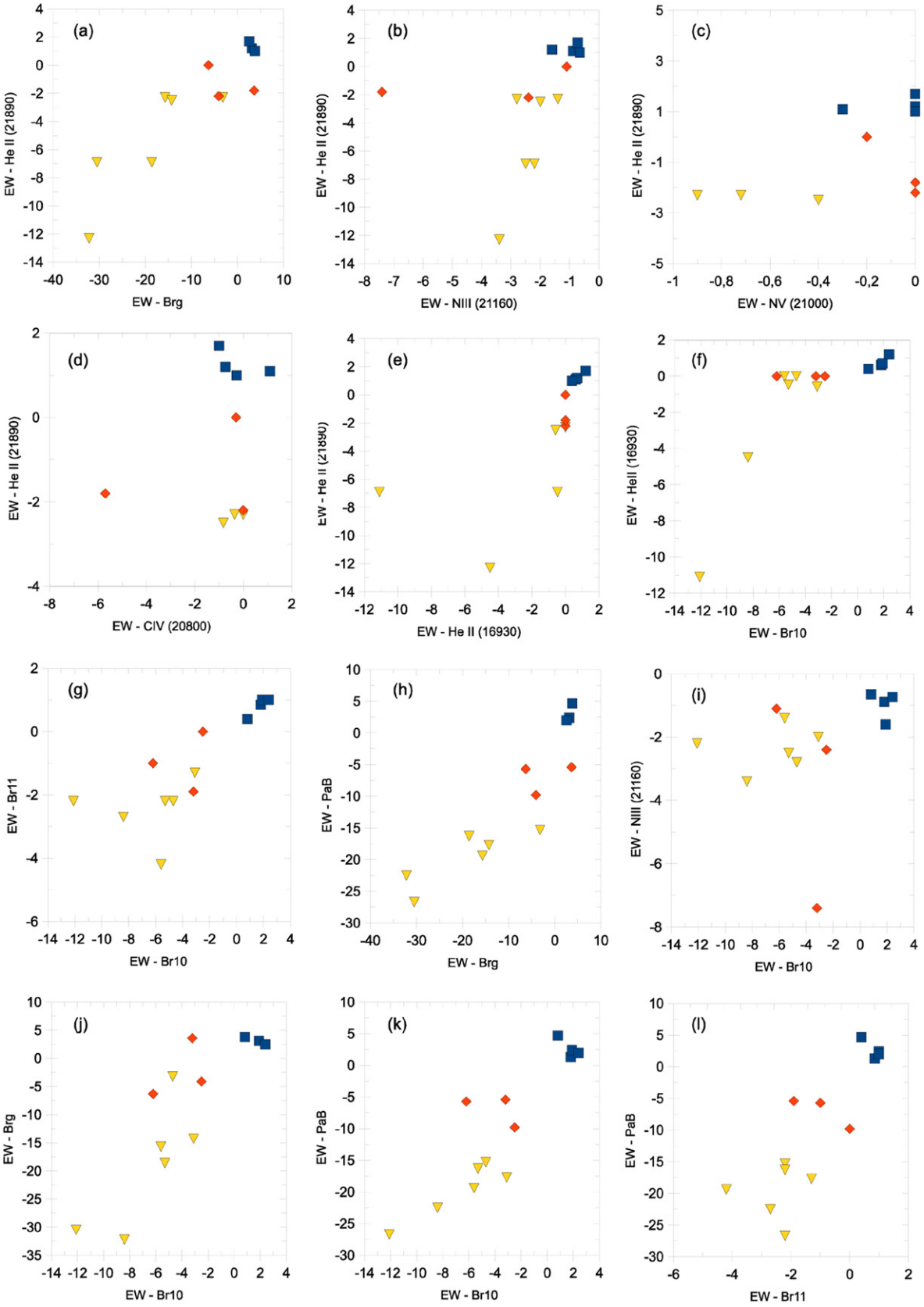

Figure 7. Observed values of EWs (Å) for O (squares), OIf* (diamonds), and OIf*/WN type (triangles) stars in Table 5. As can be seen from panels (e)–(l), the use of *H*- and *J*-band spectral line measurements can also provide a good separation of the distinct types. In fact, the combination of the Br10, Br11, and Paβ hydrogen line measurements is particularly useful when separating the transitional OIf*/WN stars from the OIf* ones. In this sense, good results are achieved using Paβ line measurements combined with the *H*-band hydrogen transitions.

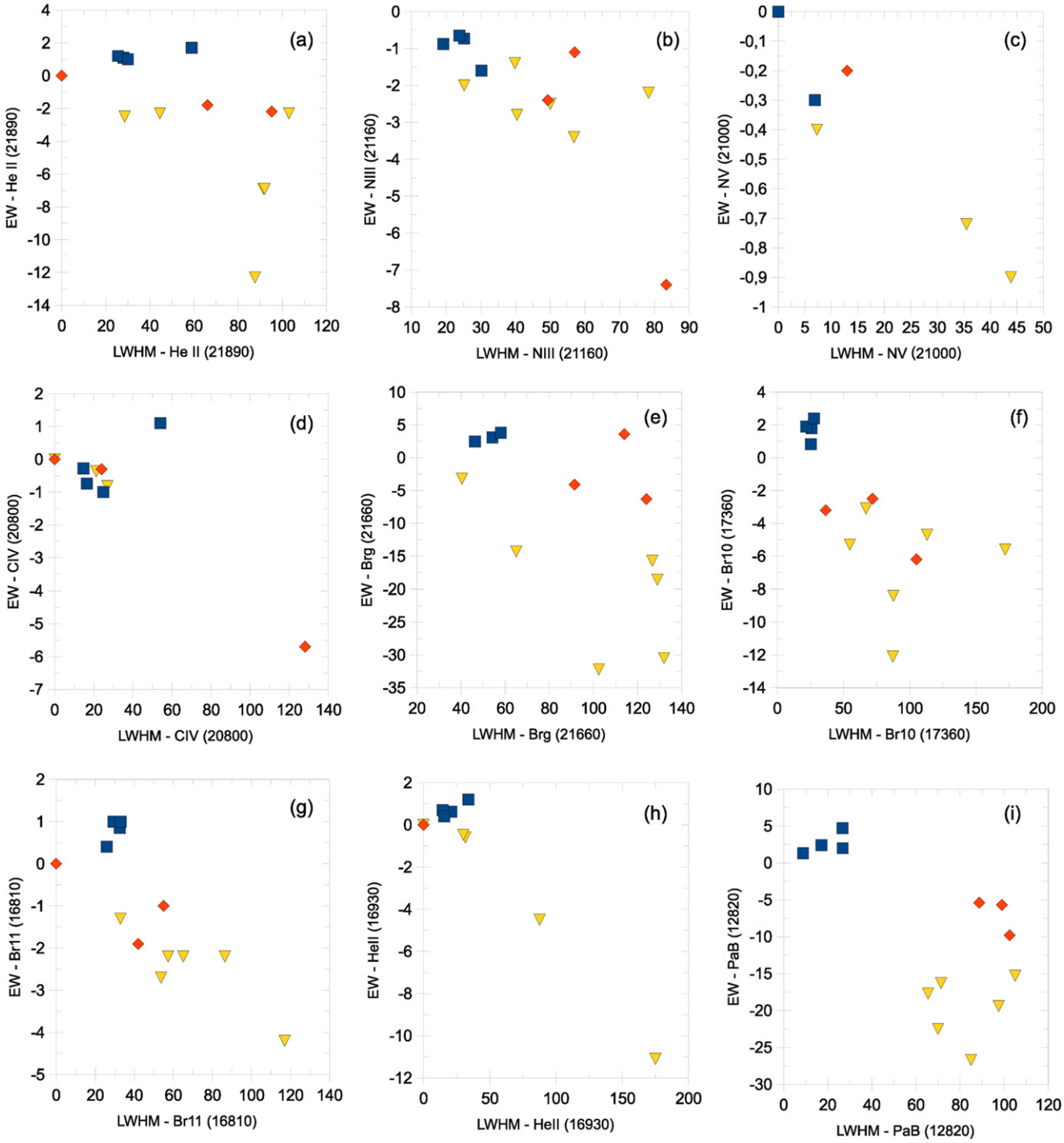

Figure 8. Observed values of EW × LWHM (Å) for the O (squares), OIf* (diamonds), and OIf*/WN type (triangles) stars in Table 5.

type stars from the OIf* group. This is particularly evident for those OIf*/WN stars presenting He II $\lambda\lambda$21890 and Brγ LW values satisfying simultaneously the condition EW (He II) < -2 Å, and EW(Brγ) < -12.5 Å, which correspond to a combined width of W_λ(Brγ+He II) ~15 Å, about half of the value suggested by Crowther & Walborn (2011) for the criterion defining the boundary between OIf* and OIf*/WN stars. On the other hand, as can be seen from figure 7(e)–(l), the use of *H*- and *J*-band spectral line measurements can also provide a good separation of the distinct types. In fact, the combination of the Br10, Br11, and Paβ hydrogen line measurements is particularly useful when separating the transitional OIf*/WN stars from the OIf* ones. In this sense, good results are achieved using Paβ line measurements combined with the *H*-band hydrogen transitions, as can be seen in figure 7(k) for EW (Paβ) × EW (Br10) and figure 7(l) for EW (Paβ) × EW (Br11).

From such diagrams one may conclude that the approximate values defining the boundaries between OIf* and OIf*/WN stars are those corresponding to combined EWs EW_λ(Brγ +paβ) > 18 Å (figure 7(h)), EW_λ(Br10+paβ) > 20 Å (figure 7 (k)), and EW_λ(Br11+paβ) > 16 Å (figure 7(l)). Finally,

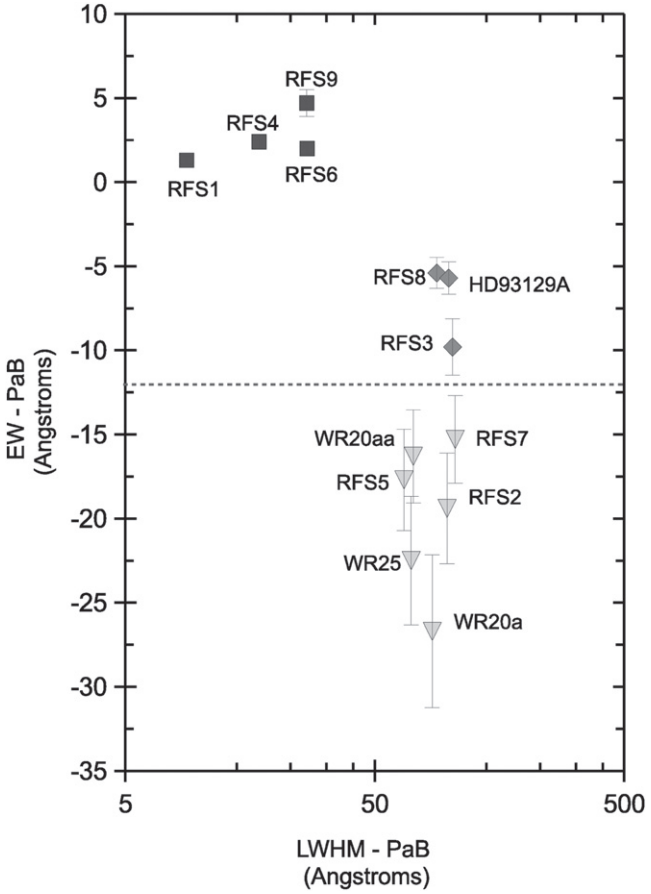

Figure 9. EW × LWHM Paβ values for O (squares), OIf* (diamonds), and OIf*/WN type (triangles) stars in Table 5. The results for the Paβ emission line indicate that the transition boundary between OIf* and OIf*/WN stars occurs for EW (Paβ) ∼ 12 Å, always for spectral lines showing LWHM (Paβ) values above ∼60 Å.

regarding the approximate boundaries between subtypes analogous to the criterion using the He II λ4686 in the optical window (Crowther & Walborn 2011), the results for the Paβ emission line are shown in Figure 9. There it is clearly seen that the transition boundary between OIf* and OIf*/WN stars occurs for EW (Paβ) ∼ 12 Å, always for lines showing LWHM (Paβ) values above ∼60 Å.

5. CONCLUDING REMARKS

In this work we performed a search for VMS candidates beyond the center of the massive stellar cluster NGC 3603, which is known to be one of the most massive, dense, and rich Galactic star-forming regions, and is believed to be a scaled version of the R136 starburst cluster in the LMC. Based on NIR color and magnitude selection criteria applied to the 2MASS PSC, the chosen stars were observed through a SOAR NIR and optical spectroscopic survey, which confirmed the existence of several massive stars in isolation in the NGC 3603 field.

From the analysis of the spectroscopic survey and related optical–NIR photometry, our main results are:

1. Three new Galactic exemplars of the OIf*/WN type, RFS2 (MTT58), RFS5 (WR42e), and RFS7, are confirmed in the periphery of NGC 3603. They are very young massive stars with probable initial masses well above 100 $M_\odot$ and estimated ages of about 1 Myr. RFS5 (O3If*/WN6–135 $M_\odot$) appears to be a bit more massive than RFS2 and RFS7, both with estimated initial masses of ∼115 $M_\odot$. Such results are in line with the estimated mass of NGC 3603-C, the O3If*/WN6 star placed in the core of the NGC 3603, which has an estimated mass of 123–154 $M_\odot$ and an absolute visual magnitude *of* $M_V = -7.2$ (Crowther et al. 2010).
2. Based on a Goodman blue-optical spectrum of RFS3 (MTT68), we may now confirm that it is indeed a highly reddened O2If* star, the only other Galactic exemplar (in addition to HD 93129A) known to date. Based on its position relative to a set of theoretical isochrons in a H–R diagram, we concluded that the new O2If* star is probably one of the most massive (150 $M_\odot$) and luminous ($M_V = -7.3$) O-stars in the Galaxy.
3. The RFS1 blue-optical spectrum is a near clone of the prototype of the O2v class, the BI 253 star in the LMC (Walborn et al. 2002), which makes RFS1 the first Galactic exemplar known to date. Based on its location on the H–R diagram, we found that it is a star with a probable initial mass of 80 $M_\odot$, and a luminosity similar to the other O2v stars found in the LMC.
4. The case of RFS8, a new Galactic O3.5If* star, is quite intriguing. It is found well to the south of the NGC 3603 complex, in apparent isolation at a large radial angular center distance of 29′, or equivalently, at a projected linear distance of about 62 pc. Based on its location in the H–R diagram and in accordance with the stellar evolutionary models, RFS8 probably had an initial mass of 77 $M_\odot$. Its derived absolute magnitude $M_V = -6.4$ is similar to that of the other O3.5If* (Sh18) found in NGC 3603's innermost region. The fact that a such high mass star is found well isolated in the field led us to speculate that it could have been expelled from the innermost parts of the complex.
5. From the spectroscopic study and associated optical and NIR photometry, we were able to derive the values of the total to selective extinction ratio R_V and the corresponding optical to NIR color excesses $E(B-V)$, $E(J-V)$, $E(H-V)$, and $E(K-V)$ for each star in our sample. Our results are consistent with the anomalous interstellar extinction law found in previous studies in the direction of the NGC 3603 region. We found a radial dependence on the total to selective extinction ratio, with the associated R_V values decreasing as a function of r_c given by $R_V = 3.881 - 0.014 r_c$.
6. Based on the EW and LW measurements taken from the observed NIR spectroscopic lines, we constructed EW and EW × LWHM comparative diagrams and found that the normal O-type stars can easily be separated from the OIf* and OIf*/WN type stars. Also, in the particular case of using only the *K*-band, it is possible not only to separate normal O-type stars from the OIf* and OIf*/WN types, but also to identify the majority of the OIf*/WN type stars that present He II $\lambda\lambda$21890 and Brγ LW values satisfying simultaneously the conditions EW(He II) < -2 Å and EW(Brγ) < -12.5 Å, which correspond to a combined width of W_λ(Brγ+He II) ∼15 Å, about half of the value suggested by Crowther & Walborn (2011).

On the other hand, in the absence of *K*-band

spectroscopic data, excellent results in the separation process are achieved using Paβ line measurements combined with those of *H*-band hydrogen Br10 and Br11 transitions. In this case the values defining the boundaries between OIf* and OIf*/WN stars correspond to the combined EWs satisfying EW$_\lambda$(Br10+paβ) > 20 Å and EW$_\lambda$(Br11+paβ) > 16 Å.

Finally, regarding the approximate boundaries between subtypes analogous to the criterion using the He II λ4686 in the optical window (Crowther & Walborn 2011), the best choice in the NIR is that using the Paβ emission line, for which we clearly see a transition boundary between OIf* and OIf*/WN stars occurring for EW (Paβ) ~ 12 Å and LWHM (Paβ) values above $\sim$60 Å.

A.R.L. is grateful for partial support from DIULS Regular project PR15143. G.A.P.F. is partially supported by CNPq and FAPEMIG. We thanks the SOAR staff for the efficient support provided during the OSIRIS and Goodman observing runs. A. R.L. thanks Dr. Nolan Walborn for stimulating discussions about the optical spectra of O2v stars. This publication makes use of data products from the Two Micron All Sky Survey, which is a joint project of the University of Massachusetts and the Infrared Processing and Analysis Center/California Institute of Technology, funded by the National Aeronautics and Space Administration and the National Science Foundation. IRAF is distributed by the National Optical Astronomy Observatory, which is operated by the Association of Universities for Research in Astronomy (AURA) under a cooperative agreement with the National Science Foundation. This work is based (in part) on observations made with the *Spitzer Space Telescope*, which is operated by the Jet Propulsion Laboratory, California Institute of Technology under a contract with NASA. This research has made use of data obtained from the *Chandra* Source Catalog, provided by the *Chandra* X-ray Center (CXC) as part of the *Chandra* Data Archive. This research has made use of the VizieR catalog access tool, CDS, Strasbourg, France. The original description of the VizieR service was published in AAS 143, 23

Facility: OSIRIS.

REFERENCES

Andersen, M., Zinnecker, H., Moneti, A., et al. 2009, ApJ, 707, 1347
Bestenlehner, J. M., Grafener, G., Vink, J. S., et al. 2014, A&A, 570, 38
Bestenlehner, J. M., Vink, J. S., Grafener, G., et al. 2011, A&A, 530, 14
Bonanos, A. Z., Stanek, K. Z., Udalski, A., et al. 2004, ApJ, 611, 33
Bressan, A., Marigo, P., Girardi, L., et al. 2012, MNRAS, 427, 127
Chini, R., & Kruegel, E. 1983, A&A, 117, 289
Chini, R., & Wargau, W. F. 1990, A&A, 227, 213
Crowther, P., & Walborn, N. 2011, MNRAS, 416, 1311
Crowther, P. A., Schnurr, O., Hirschi, R., et al. 2010, MNRAS, 408, 731
de Koter, A., Heap, S. R., & Hubeny, I. 1997, ApJ, 477, 792
Fedorov, P. N., Akhmetov, V. S., Bobylev, V. V., & Gontcharov, G. A. 2011, MNRAS, 415, 665
Fitzpatrick, E. L. 1999, PASP, 111, 63
Gvaramadze, V. V., & Gualandris, A. 2011, MNRAS, 410, 304
Gvaramadze, V. V., Kniazev, A. Y., Chene, A.-N., & Schnurr, O. 2013, MNRAS, 430, L20
Hanson, M. M., Conti, P. S., & Rieke, M. J. 1996, ApJS, 107, 281
Hanson, M. M., Kudritzki, R.-P., Kenworthy, M. A., Puls, J., & Tokunaga, A. T. 2006, ApJS, 161, 154
Hur, H., Sung, H., & Lim, B. 2014, ASPC, 482, 239
Lamers, H. J. G. L. M., & Cassinelli, J. P. 1999, Introduction to Stellar Winds (Cambridge: Cambridge Univ. Press)
Martins, F., & Plez, B. 2006, A&A, 457, 637
Martins, F., Schaerer, D., Hillier, D. J., et al. 2005, A&A, 441, 735
Massey, P., Puls, J., Pauldrach, A. W. A., et al. 2005, ApJ, 627, 477
Melena, M. W., Massey, P., Morrell, N. I., & Zangari, A. M. 2008, AJ, 135, 878
Melnick, J., Tapia, M., & Terlevich, R. 1989, A&A, 213, 89
Moffat, A. F. J., Corcoran, M. F., Stevens, I. R., et al. 2002, ApJ, 573, 191
Moffat, A. F. J., Shara, M. M., & Potter, M. 1991, AJ, 102, 642
Neckel, T., & Chini, R. 1981, A&A, 45, 451
Niemela, V. S., Gamen, R. C., Barba, R. H., et al. 2008, MNRAS, 389, 1447
Pandey, A. K., Ogura, K, & Sekiguchi, K 2000, PASJ, 52, 847
Rauw, G., De Becker, M., Nazao, Y., et al. 2004, A&A, 420, L9
Rauw, G., Vreux, J.-M., Gosset, E., et al. 1996, RMxAC, 5, 108
Repolust, T., Puls, J., & Herrero, A. 2004, A&A, 415, 349
Rochau, B., Brandner, W., Stolte, A., et al. 2010, ApJ, 717, 90
Roeser, S., Demleitner, M., & Schilbach, E. 2010, AJ, 139, 2440
Roman-Lopes, A. 2009, MNRAS, 398, 1368
Roman-Lopes, A. 2012, MNRAS, 427, 65
Roman-Lopes, A. 2013a, MNRAS, 433, 712
Roman-Lopes, A. 2013b, MNRAS, 435, 73
Roman-Lopes, A., Barba, R., & Morrell, N. 2011, MNRAS, 416, 501
Romano, P., Campana, S., Mignani, R. P., et al. 2008, A&A, 488, 1221
Rosslowe, C. K., & Crowther, P. A. 2015, MNRAS, 447, 2322
Sabín-Sanjulián, C., Simón-Díaz, S., Herrero, A., et al. 2014, A&A, 564, 39
Sana, H., Gosset, E., & Evans, C. J. 2009, MNRAS, 400, 1479
Schnurr, O., Casoli, J., Chenè, A.-N., Moffat, A. F. J., & St-Louis, N. 2008, MNRAS, 389, 38
Schnurr, O., Moffat, A. F. J., Villar-Sbaffi, A., St-Louis, N., & Morrell, N. 2009, MNRAS, 395, 823
Shara, M. M., Smith, L. F., Potter, M., & Moffat, A. F. J. 1991, AJ, 102, 642
Simon, K. P., Kudritzki, R. P., Jonas, G., & Rahe, J. 1983, A&A, 125, 34
Skrutskie, M. F., Cutri, R. M., Stiening, R., et al. 2006, AJ, 131, 1163
Smith, L. F., Shara, M. M., & Moffat, A. F. J. 1996, MNRAS, 281, 163
Smith, N., & Conti, P. S. 2008, ApJ, 679, 1467
Sota, A., Maíz Apellániz, J., Morrell, N. I., et al. 2014, ApJ, 211, 10
Sota, A., Maíz Apellániz, J., Walborn, N. R., et al. 2011, ApJS, 193, 24
Sung, H., & Bessell, M. S. 2004, AJ, 127, 1014
Taresch, G., Kudritzki, R. P., Hurwitz, M., et al. 1997, A&A, 321, 531
Townsley, L. K., Broos, P. S., Garmire, G. P., et al. 2014, ApJS, 213, 1
Vink, J. S., Heger, A., Krumholz, M. R., et al. 2015, HiA, 16, 51
Walborn, N. 1982, ApJ, 254, 15
Walborn, N., & Blades, C. 1997, ApJS, 112, 457
Walborn, N., Howarth, I. D., Lennon, D. J., et al. 2002, AJ, 123, 2754
Walborn, N., Sana, H., Simoń-Diáz, S., et al. 2014, A&A, 564, 40
Wegner, W. 2005, MNRAS, 371, 185
XMM-Newton Survey Science Centre 2013, yCat, 9044, 0
Zacharias, N., Finch, C. T., Girard, T. M., et al. 2013, AJ, 145, 44
Zacharias, N., Monet, D. G., Levine, S. E., et al. 2004, AAS, 205, 4815